

Implementation of an Efficient Pressure-Based CFD Solver for Accurate Thermoacoustic Computations

J.-M. Lourier*, M. Di Domenico†, B. Noll† and M. Aigner‡

German Aerospace Center (DLR), Institute of Combustion Technology

Pfaffentalring 38-40, 70596, Stuttgart, Germany

The implementation of a semi-implicit pressure-based fractional step method for compressible flows, and the incorporation of characteristic boundary conditions (NSCBC) is described. The discussion focuses on the discretisation of the pressure correction equation and the characteristic boundary conditions with respect to convergence rate of the algorithm and accuracy of the boundary conditions. An implicit implementation of the NSCBC is shown which removes the acoustic CFL limitation at boundaries while retaining the accuracy of the NSCBC approach. In this context, a new extrapolation method based on the Green-Gauss approach is proposed.

I. Introduction

WITHIN the last decade innovative combustion technologies have been developed to reduce environmental pollution. For instance, lean premixed combustion results in a lower flame temperature, and hence in less thermal nitric oxide. However, lean combustion increases the susceptibility to thermoacoustic instabilities.¹ These instabilities can cause operational difficulties or even destroy the combustor.² Therefore, the suppression of thermoacoustic instabilities is of growing importance for the design process of combustion chambers. Since a full scale experimental analysis of instabilities is very expensive, computational fluid dynamics (CFD) has become a promising tool to predict thermoacoustic instabilities.

The solving strategy pursued within CFD codes for combustion prediction is mostly driven by two key aspects. Firstly, the flow speed within industrially applied combustion chambers is usually within the incompressible regime, i.e. the Mach number is low. These low Mach number flows are traditionally simulated by preconditioned density-based or pressure-based solvers.³ Secondly, combustion simulation is remarkably more expensive than cold flow computation due to a higher number of transport equations which have to be solved for accurate combustion predictions. Since pressure-based solvers commonly require lower computational effort than preconditioned density-based solvers, the majority of CFD codes used for combustion simulations invoke a pressure-based solver.⁴

Pressure-based solvers have been developed initially with the assumption of an incompressible flow where pressure and density variations are decoupled. This decoupling results in infinite propagation speed of pressure oscillations which eventually precludes the computation of thermoacoustic instabilities. Many extensions of pressure-based implicit solvers towards compressible flows have been developed. However, most of these extensions suffer from low temporal order of accuracy or require costly inner loop iterations to converge to a time-accurate solution.³ Moureau et al. proposed a pressure-based method, which is second order accurate for linear acoustics and low Mach advection without inner loop iterations.³ The semi-implicit compressible solver invokes a fractional step method⁵⁻⁷ based on characteristic splitting of acoustic and advective modes. The corrector step solves a Helmholtz equation and contains purely the acoustic modes of the flow. Advective modes are solved within the predictor step. This allows for adapted numerical treatments of the different modes.

Since the semi-implicit characteristic splitting (SICS) solver is a promising algorithm for thermoacoustic computations due to its low computational costs and high accuracy, it has been implemented in the DLR

*PhD Student, DLR, Institute of Combustion Technology, Stuttgart, Germany.

†Research Engineer, DLR, Institute of Combustion Technology, Stuttgart, Germany.

‡Professor, DLR, Institute of Combustion Technology, Stuttgart, Germany.

THETA⁸ code. THETA is a finite volume solver for unstructured grids optimised for combustion prediction. It was initially designed to compute incompressible reacting flows. In this paper, details concerning the implementation of the compressible solver are presented. In this context, different numerical treatments of the Helmholtz equation and its boundary conditions are discussed with respect to convergence rate of the algorithm. Furthermore, the solver's accuracy regarding the prediction of acoustic wave propagation is compared to other compressible solvers.^{4,9} Finally, results of a test case involving entropy and acoustic wave interactions are presented and compared to experimental as well as cross-solver numerical data.¹⁰

II. Fractional Step Method

THE Navier-Stokes equations for compressible flows are solved by means of a fractional step method⁵⁻⁷ proposed by Moureau et al.,³ which is called semi-implicit characteristic splitting (SICS) solver in the following. Generally speaking, fractional step methods split a physical time step into multiple computational steps, e.g. into a predictor and a corrector step. The operators of the underlying equations are decomposed, and solved separately within the different computational steps.⁶ In case of SICS, the Navier-Stokes equations are decomposed by means of a characteristic splitting into acoustic and advective modes. In the following sections, this characteristic splitting is shown and the discretisation of the resulting Helmholtz equation, i.e. the pressure correction equation, is discussed.

II.A. Characteristic Splitting

The Navier-Stokes equations for compressible flows can be arranged as:³

$$\frac{\partial \rho}{\partial t} + \rho \nabla \cdot u + \underline{u \cdot \nabla \rho} = 0, \quad (1)$$

$$\frac{\partial \rho u}{\partial t} + \rho u \nabla \cdot u + \underline{u \cdot \nabla \rho u} = \underline{-\nabla p} + \nabla \cdot \mathbf{t} \quad \text{and} \quad (2)$$

$$\frac{\partial \rho h}{\partial t} + \rho h \nabla \cdot u + \underline{u \cdot \nabla \rho h} = \underline{-c^2 \rho \nabla \cdot u} + \gamma \nabla \cdot (\lambda \nabla T) + \gamma \mathbf{t} \cdot \nabla u, \quad (3)$$

where ρ is the density, u the velocity, h the sensible enthalpy, p the pressure, T the temperature, c the speed of sound, \mathbf{t} the total stress tensor, λ the thermal conductivity and γ the heat capacity ratio. This system of equations is decomposed into acoustic and advective modes. First of all, the underlined terms in equations (1)-(3) are neglected, which results in the advection system of equations:

$$\frac{\phi^* - \phi^n}{\Delta t} + u \cdot \nabla \phi = D_\phi \quad (4)$$

where ϕ is $[\rho, \rho u, \rho h]$ and D_ϕ is $[0, \nabla \cdot \mathbf{t}, \gamma \nabla \cdot (\lambda \nabla T) + \gamma \mathbf{t} \cdot \nabla u]$. ϕ^* is an intermediate solution. Neglecting the diffusion and dissipation terms D_ϕ allows for a one-dimensional characteristic analysis,¹¹ which shows that the eigenvalues of (4) are $[u, u, u]$. Hence, all disturbances governed by the set of equations (4) propagate with flow velocity u .

Subtracting (4) from (1)-(3) gives the acoustic system of equations:³

$$\frac{\phi^{n+1} - \phi^*}{\Delta t} + \nabla \phi \cdot u = R_\phi \quad (5)$$

where R_ϕ is $[0, -\nabla p, -c^2 \rho \nabla \cdot u]$. The eigenvalues of equation (5) amount to $[-c, 0, c]$, which proofs that only the propagation of acoustic disturbances are computed by means of this system of equations.

As mentioned above, the advective and acoustic systems are used as predictor and corrector step, respectively, of the fractional step method SICS. Within the predictor step, equations (4) are solved subsequently in a semi-implicit way. By contrast, the acoustic system is solved implicitly to remove the acoustic CFL limitation.³ For this reason equations (5) are transposed to form a Helmholtz equation:³

$$\nabla \cdot \nabla \delta p - \nabla \cdot \left(\frac{2u^{n+1/2}}{c^2 \Delta t} \delta p \right) - \frac{4}{c^2 \Delta t^2} \delta p = -\nabla \cdot \nabla(p^n + p^*) + \frac{4}{\Delta t} \left(\frac{\rho^* - \rho^n}{\Delta t} + \nabla \cdot \left(\frac{\rho u^* + \rho u^n}{2} \right) \right) \quad (6)$$

where δp is the pressure correction, which reads:

$$\delta p = p^{n+1} - p^*. \quad (7)$$

As part of the derivation of equation (6) the continuity equation (1) is used. Hence, solving the Helmholtz equation ensures inherently mass conservation. The full solution algorithm is shown by Moureau et al.³

II.B. Discretisation of the Helmholtz equation

The Helmholtz equation (6) is solved implicitly to remove the acoustic CFL limitation. In accordance with this, the discretisation of the last term on the LHS is fully specified. However, there are several numerical treatments possible for the Laplacian and the convective-type discretisation operators of equation (6). In case of a finite volume solver with collocated variable arrangement as considered here, the computation of a Laplacian and a convective operator reduces to the computation of a cell face normal gradient (F_G) and a convective flux (F_C) through the cell face, respectively. The estimation of both face values is discussed in the following.

The deferred correction is commonly used for the computation of the pressure gradient at cell faces.^{12–14} Following this approach, the gradient is estimated by means of the adjoined values at the cell centers and the mean pressure gradient, i.e.:

$$F_G = \nabla p^m \cdot (\alpha s) + \bar{\nabla} p^{m-1} \cdot (n - \alpha s), \quad (8)$$

$$\nabla p^m \cdot s = \frac{1}{|l|}(p_1^m - p_0^m) \text{ and} \quad (9)$$

$$\bar{\nabla} p^{m-1} = \frac{1}{2}(\nabla p_0^{m-1} + \nabla p_1^{m-1}) \quad (10)$$

where s is the unit vector between cell face adjoined points, n the unit cell face normal vector, α a scaling factor, $|l|$ the distance between the face adjoined cell centroids and m the iteration index (Fig. 1). The scaling factor α is arbitrary. Initially a scaling factor of $\alpha = 1$ was used by Ferziger and Peric.¹³ Traore¹⁵ found that a factor of $\alpha = 1/\cos\theta$, where θ is the inner face angle (Fig. 1), results in a more stable algorithm for highly skewed grids. Hence, the proposed value of Traore¹⁵ is used.

The pressure gradient computed from adjoined cell values is implicitly computed at the current iteration m . Whereas the mean pressure gradient $\bar{\nabla} p$ is computed from last iteration values, i.e. either from the last inner iteration or from the last physical time step. This explicit treatment reduces the computational costs, since the pressure gradient at cell centroids needs only to be computed once before each iteration. However, a fully implicit treatment of both terms has been found to highly increase the convergence rate of the pressure correction equation as discussed in section IV.A.

As presented for the Laplacian of the Helmholtz equation (6), the convective-like term can also be discretised in many different ways.^{13,16} According to the experience, upwind biased schemes produce accurate and robust solutions in case of incompressible flows. Therefore, a quadratic upwind scheme (QUDS)¹³ is used to discretise the convective Helmholtz term of the compressible solver. In addition, the central difference scheme (CDS)¹³ is utilised. The influence of these different discretisations on dispersion and dissipation errors is discussed in section IV.B.

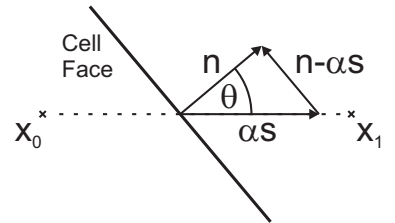


Figure 1. Deferred correction.

III. Characteristic Boundary Conditions

THE computational domain of a CFD simulation usually only comprises a part of the physical domain due to limitations of computational resources and turn around times.¹⁷ Therefore, artificial boundaries have to be introduced. In case of a hyperbolic systems, such as the Helmholtz equation discussed here, artificial boundaries are usually derived from the analysis of different waves crossing the boundary.¹⁸ The classical approach for this are the Navier-Stokes Characteristics Boundary Conditions (NSCBC).¹⁹ Generally speaking, characteristic equations are solved at boundaries allowing for a separate treatment of boundary crossing waves.

The classical NSCBC method involves a explicit integration of the characteristic equations, which results in a CFL limitation at the boundary adjoined cells.³ To remove this CFL limitation at boundaries, the characteristic equations are solved implicitly by means of Dirichlet boundary conditions. In the following this method is shown.

III.A. Characteristic Helmholtz Equation

To derive the characteristic Helmholtz equation, the underlying equations have to be written in characteristic form. A characteristic analysis^{11,18} of the Navier-Stokes equations (1)-(3) shows that five characteristic waves L_i cross inlet and outlet boundaries as illustrated in figure 2(a). They amount to the associated eigenvalues λ_i multiplied by the characteristic wave amplitude, and are given by:^{17,18}

$$L_1 = \lambda_1 \left(\frac{\partial p}{\partial x_1} - \rho c \frac{\partial u_1}{\partial x_1} \right), \quad (11)$$

$$L_2 = \lambda_2 \left(c^2 \frac{\partial \rho}{\partial x_1} - \frac{\partial p}{\partial x_1} \right), \quad (12)$$

$$L_3 = \lambda_3 \frac{\partial u_2}{\partial x_1}, \quad (13)$$

$$L_4 = \lambda_4 \frac{\partial u_3}{\partial x_1} \quad \text{and} \quad (14)$$

$$L_5 = \lambda_5 \left(\frac{\partial p}{\partial x_1} + \rho c \frac{\partial u_1}{\partial x_1} \right). \quad (15)$$

Where x_1 is the boundary normal coordinate and u_i the velocity component in x_i direction. Each characteristic wave L_i is associated to a physical quantity propagated at the speed λ_i through the flow. L_1 and L_5 are the acoustic pressure waves, L_2 is the advective entropy wave whereas L_3 and L_4 are associated with advective waves of the velocity components u_2 and u_3 , respectively.¹⁸ The fractional step method SICS involves a splitting of the acoustic and advective waves. Therefore, the characteristic waves of the predictor (4) and corrector (5) step differ from the waves of the full Navier-Stokes equations in the eigenvalues λ_i , whereas the wave amplitudes remain the same. The eigenvalues of the three systems of equations and the corresponding characteristic waves are shown in figure 2.

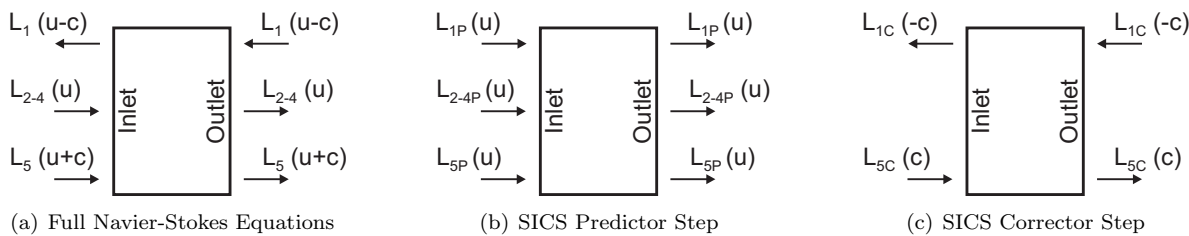


Figure 2. Characteristics waves at inlet and outlet boundaries for a subsonic flow.

The characteristic waves (11)-(15) are substituted into the acoustic system of equations (5) and the continuity equation (1) to replace the derivatives in x_1 -direction. Using these equations, the characteristic Helmholtz equation is derived in the same way as the previously shown Helmholtz equation (6). The terms involving a derivative in boundary normal direction x_1 of the characteristic Helmholtz equation are given by:

$$\frac{\partial^2 \delta p}{\partial x_1^2} = \frac{\partial}{\partial x_1} \left(\frac{L_{5C}^\delta - L_{1C}^\delta}{2c} \right), \quad (16)$$

$$\frac{\partial u^{n+1} \delta p}{\partial x_1} = u_1^{n+1/2} \left(\frac{L_{5C}^\delta + L_{1C}^\delta}{2c} \right) + \delta p \left(\frac{L_{5C}^{n+1/2} - L_{1C}^{n+1/2}}{2\rho c} \right), \quad (17)$$

$$\frac{\partial^2 p^n}{\partial x_1^2} = \frac{\partial}{\partial x_1} \left(\frac{L_{5C}^n - L_{1C}^n}{2c} \right), \quad (18)$$

$$\frac{\partial^2 p^*}{\partial x_1^2} = \frac{\partial}{\partial x_1} \left(\frac{L_{5C}^* - L_{1C}^*}{2c} \right), \quad (19)$$

$$\frac{\partial \rho u^*}{\partial x_1} = \frac{L_{5C}^* + L_{1C}^*}{2c^2} \quad \text{and} \quad (20)$$

$$\frac{\partial \rho u^n}{\partial x_1} = \frac{1}{c^2} \left(L_2^n + \frac{1}{2}(L_5^n + L_1^n) \right) \quad (21)$$

where the time level δ , e.g. L_i^δ , is computed as difference between the waves at new and advected time level:

$$L_i^\delta = L_i^{n+1} - L_i^*. \quad (22)$$

Substituting equations (16)-(21) into (6) gives the characteristic Helmholtz equation, which is solved at boundaries according to the NSCBC method.

The key advantage of the characteristic equation is the ability to compute the characteristic waves crossing a boundary separately. Following characteristics theory,²⁰ outgoing waves are computed from inner points since information propagates out of the computational domain. Incoming waves are either computed from known information about the outside of a domain or they have to be approximated.¹⁸ Among others, incoming waves are sent in to avoid a drift in mean flow values, e.g. to apply the far field pressure at an outlet boundary. In this scope, Poinsot and Lelle¹⁹ proposed to set the incoming wave amplitude to

$$L_{in} = K(p - p_\infty) \quad \text{with} \quad (23)$$

$$K = \sigma c(1 - Ma^2)/L. \quad (24)$$

Where K is a relaxation coefficient, p the predicted pressure, p_∞ the far field pressure, σ a coupling parameter, c the speed of sound, Ma a reference Mach number and L a reference length. Applying the incoming wave (23) reduces the drift of mean values with increasing relaxation coefficient of the boundary condition, i.e. with increasing K . However, increasing the relaxation coefficient also increases the reflection at the boundary. The magnitude of the analytical reflection factor reads:²¹

$$||R|| = \frac{1}{\sqrt{1 + \left(\frac{2\omega}{K}\right)^2}} \quad (25)$$

where R is the reflection factor and ω the angular frequency. This analytical expression of the reflection factor is used in section IV.C to asses the accuracy of the implemented boundary conditions.

III.B. Extrapolation Methods

The characteristic Helmholtz equation derived in section III.A is solved implicitly within the boundary adjoined cells (fig. 3). In this scope, the boundary normal gradients defined by equations (16)-(21) are used to extrapolate pressure and velocity values on the boundaries. These values are then used in turn as Dirichlet boundary conditions of the characteristic Helmholtz equation.

The extrapolation to the boundary points can be done by a linear extrapolation, i.e. in case of pressure the boundary value is given by:

$$p_b = p_0 + \nabla p_b \cdot s \quad (26)$$

where p_b is the boundary pressure value, p_0 is the pressure in the boundary cell centroid, ∇p_b is the pressure gradient at the boundary and s is the distance between the cell centroid x_0 and the boundary point x_b (fig. 3). The pressure gradient at the boundary amounts to the characteristic gradient ∇_{ch} in boundary normal direction, and hence is given by:

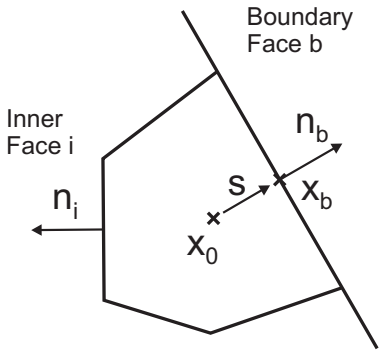


Figure 3. Boundary adjoined cell.

$$\nabla p_b = \nabla p_0 + ((\nabla p)_{ch} - \nabla p_0 \cdot n)n. \quad (27)$$

In summary, the boundary normal gradients are computed from characteristic waves. These gradients are used to set Dirichlet boundary conditions for the Helmholtz equation by means of linear extrapolation. However, this does not ensure that the characteristic gradient is exactly applied within the boundary adjoined cell for the characteristic Helmholtz equation. For this reason, another new method called Green-Gauss reconstruction is proposed here. The boundary normal gradient in the adjoined cell is given by the Green-Gauss method as:

$$\nabla p \cdot n_b = \frac{1}{V_0} \left(\sum_i (p_i n_i \cdot n_b A_i) + p_b n_b \cdot n_b A_b \right), \quad (28)$$

where n_b is the boundary normal unit vector, V_0 the cell volume of the adjoined cell, p_i the pressure value at an inner face, n_i the normal unit vector at an inner face, A_i the inner face area, p_b the boundary pressure value and A_b the boundary face area (fig. 3). From equation (28) the boundary value p_b amounts to:

$$p_b = \frac{1}{A_b} \left(V_0 \nabla p \cdot n_b - \sum_i (p_i n_i \cdot n_b A_i) \right), \quad (29)$$

where the boundary normal gradient is computed from the characteristic waves, i.e.:

$$\nabla p \cdot n_b = (\nabla p)_{ch}. \quad (30)$$

Using equation (29) as extrapolation method ensures that the gradient determined by the characteristic waves is applied within the boundary adjoined cells when the characteristic Helmholtz equation is solved. An analysis in terms of accuracy of Green-Gauss reconstruction method compared to linear extrapolation is shown in section IV.C.

III.C. Incoming Correction Wave

Following characteristic boundary theory,²⁰ domain leaving waves are computed from inner points. By contrast, domain entering waves are computed from known values of the outside of the domain,¹⁸ e.g. far field values or external forcing. Since the value of the domain entering wave L_{in} is known exactly, the respective numerical error within the boundary adjoined cells can be computed by

$$L_{in,err} = L_{in,num} - L_{in} \quad (31)$$

where L_{in} and $L_{in,num}$ are the imposed and the numerical incoming waves, respectively. The numerical incoming wave is computed from pressure and velocity gradients within the boundary adjoined cells. This error estimation is used as control variable by applying the correction wave

$$L_{in,corr}^m = -L_{in,err}^{m-1} \quad (32)$$

as additional forcing function. The error is approximated from the last time step or last inner iteration. This measure gives a higher accuracy when imposing external values as discussed in section IV.C.

IV. Results

Within the preceding sections, the fractional step method SICS was introduced, and different measures used for the implementation of SICS within the DLR THETA code were presented. In the following subsections, the impact of these measures is discussed. Finally, results of the Entropy Wave Generator (EWG) test case of Bake et al.¹⁰ are shown as validation of the implementation.

IV.A. Convergence of the Helmholtz Equation

As discussed in subsection II.B, the Laplacian of the Helmholtz equation can be discretised in a partially or fully implicit way. To examine the impact of the two different discretisations, the convergence rate of the Helmholtz equation is discussed in the following.

The convergence of the Helmholtz equation is evaluated by means of the computation of a one dimensional flow within a duct of 1 m length with a mean flow Mach number of $Ma = 0.15$. A sinusoidal pressure wave with 10 Pa amplitude and 0.1 m wave length is used as initial condition. Each wave is spatially resolved with 100 support nodes.

The fractional step method SICS is second order accurate for linear acoustics and low Mach advection without any inner iteration loop.³ However, inner iterations can be introduced to increase robustness or to retain second order accuracy at higher Mach flows. For the convergence test case, three inner iterations are computed. The convergence criterion is given by:

$$res(\delta p)_m^3 / res(\delta p)_0^1 < 10^{-5}. \quad (33)$$

Where $res(\delta p)_m^3$ is the final residual of the Helmholtz equation in the third inner iteration, and $res(\delta p)_0^1$ is the starting residual of the first inner iteration. Hence, the residual of the Helmholtz equation has to be reduced by five orders of magnitude to meet the convergence criterion. The Helmholtz equation is solved by a preconditioned BiCGstab (PBCGS) linear solver.²²

Figure 4 shows the number of iterations of the linear solver required to meet the convergence criterion described above within the first 10 time steps of the test case for different acoustic CFL numbers. With increasing acoustic CFL number the number of iterations increases. In section II.B different temporal discretisations, i.e. partially and fully implicit, were introduced. The considered test case shows that with a fully implicit discretisation the number of PBCGS iterations is significantly decreased. At a CFL number of 25, the number of linear solver iterations is around two orders of magnitude lower in case of a fully implicit discretisation.

IV.B. Dissipation and Dispersion Error

Föller and Polifke set up a test case to estimate the acoustic dissipation and dispersion error of spatial discretisations.⁹ The dissipation ϵ_p and dispersion ϵ_λ are evaluated as the relative difference of the predicted

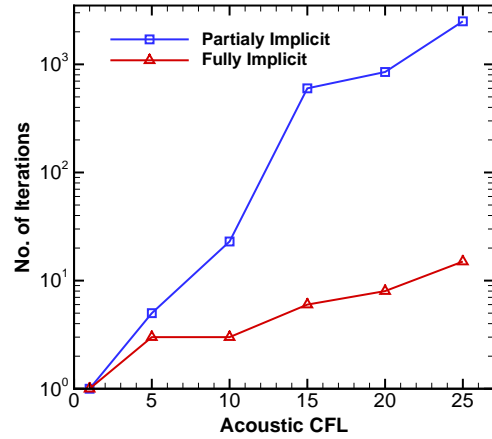


Figure 4. Convergence of Helmholtz equation.

and exact pressure amplitude and wave length, respectively, i.e.:

$$\epsilon_{\hat{p}} = \frac{\hat{p} - \hat{p}_{num}}{\hat{p}} \quad \text{and} \quad (34)$$

$$\epsilon_{\lambda} = \frac{\lambda - \lambda_{num}}{\lambda}. \quad (35)$$

Where \hat{p} , \hat{p}_{num} , λ and λ_{num} are the exact pressure amplitude, the predicted amplitude, the exact wave length and the predicted wave length, respectively. The dissipation and dispersion errors are measured after a 100 Hz sine wave with amplitude of 0.2 m/s was propagated a distance of 10 wave lengths in a one-dimensional duct with mean flow velocity of 0.25 m/s. The sine waves are spatially resolved by 10 to 40 points per wave length (PPW).

Föller and Polifke computed the error of the second order Lax-Wendroff (LW) scheme implemented into the AVPB²³ solver.⁹ Moreover, Gunasekaran and McGuirk used the test case to asses the error of the second order Total Variation Diminishing (TVD) and fifth order weighted essentially non-oscillatory (WENO) schemes.⁴ As part of this discussion, the acoustic error is computed for the second order schemes QUDS and CDS implemented in DLR THETA code (sec. II.B).

Table 1 shows the dispersion and dissipation errors of the above mentioned schemes. First of all, discretising with either QUDS or CDS has a minor influence on the acoustic error. The maximum difference between QUDS and CDS is visible at 10 PPW and amounts to roughly 0.25 % and 0.5 % in dispersion and dissipation, respectively. Furthermore, both discretisations show a dispersion error comparable to the LW scheme. Whereas, TVD and WENO show much lower dispersion errors compared to the former two schemes. The highest difference is visible at 10 PPW, where the dispersion error of TVD is around 20 times lower compared to QUDS and CDS. Regarding the dissipation, QUDS and CDS show also comparable errors as the Lax-Wendroff scheme. However, at 10 PPW QUDS shows the lowest dissipation of all schemes. The overall lowest dissipation is observed for WENO at 40 PPW and amounts to 0.2 %. In this case, the dissipation of QUDS and CDS is around 3.5 times higher compared to the WENO scheme.

Table 1. Acoustic dispersion and dissipation error of different spatial discretisations.

PPW	Dispersion Error [%]					Dissipation Error [%]				
	QUDS	CDS	LW ⁹	TVD ⁴	WENO ⁴	QUDS	CDS	LW ⁹	TVD ⁴	WENO ⁴
10	0.403	0.404	2.89	0.02	0.04	8.117	8.082	34.70	23.20	14.70
20	0.084	0.084	0.08	0.02	0.03	2.644	2.641	2.80	5.40	1.70
30	0.039	0.039	0.05	0.02	0.02	1.670	1.669	1.20	1.50	0.60
40	0.035	0.035	0.05	0.02	0.02	0.709	0.708	0.40	0.60	0.20

IV.C. Accuracy of Characteristic Boundary Conditions

In sections III.B and III.C, varying implementations of the characteristic boundary conditions, i.e. extrapolation methods and a correction wave, are discussed. To measure the impact of these implementation variants on the accuracy of the boundary conditions, the analytical expression of the reflection factor R (sec. III.A) is compared to the corresponding numerical values in this section. The analysed configurations are summarised in table 2.

To compute the reflection factor numerically, a one-dimensional flow in a duct of 1 m length with a mean flow velocity of 10m/s is simulated. A sinusoidal pressure distribution with a frequency of 1 kHz and an amplitude of 20 Pa is set as initial condition. This leads to up- and a downstream propagating waves within the duct, which are resolved spatially with 100 grid points per wave. The time steps are solved without inner iteration loops. The numerical reflection factor at inlet and outlet boundaries is then computed from:

$$\|R_{num}\| = \frac{\hat{L}_{in}}{\hat{L}_{out}}. \quad (36)$$

where \hat{L}_{in} and \hat{L}_{out} are the amplitudes of incoming and outgoing acoustic waves, respectively. At both, the inlet and outlet boundaries, the relaxation coefficient K is varied instead of the frequency of the initial pressure waves. This is a more convenient approach.²¹ The value of K is varied between 10^2 and 10^5 . The lower limit of K corresponds roughly to a coupling parameter of $\sigma = 0.27$ which is the theoretically derived optimum.²⁴ Whereas, a K value of 2×10^2 is equal to the best practise value of $\sigma = 0.58$.^{18,19} The upper limit of the considered K values results in an almost fully reflective boundary condition.

Table 2. Configurations analysed in view of boundary reflection.

Configuration	Extrapolation method	Correction Wave
Baseline	Green-Gauss	on
w/o Correction Wave	Green-Gauss	off
Linear Extrapolation	Linear	on

Figure 5 shows the modulus of the reflection factor R as a function of the relaxation coefficient K at an acoustic CFL number of unity for the three configurations shown in table 2. For the baseline configuration the predicted reflections agree well with the analytical solution for inlet (fig. 5(a)) and outlet (fig. 5(b)) boundaries. The maximum deviation is visible at $K = 10^2$ and amounts to about 3.6×10^{-3} and 1.2×10^{-3} at the inlet and outlet boundaries, respectively. In case of the configurations without correction wave and with linear extrapolation, this deviation from the analytical solution rises. Turning off the correction wave increases the maximum deviation by 64% and 170% at inlet and outlet boundaries, respectively. Changing the extrapolation method from Green-Gauss method to linear extrapolation, increases the maximum discrepancies by about one order of magnitude.

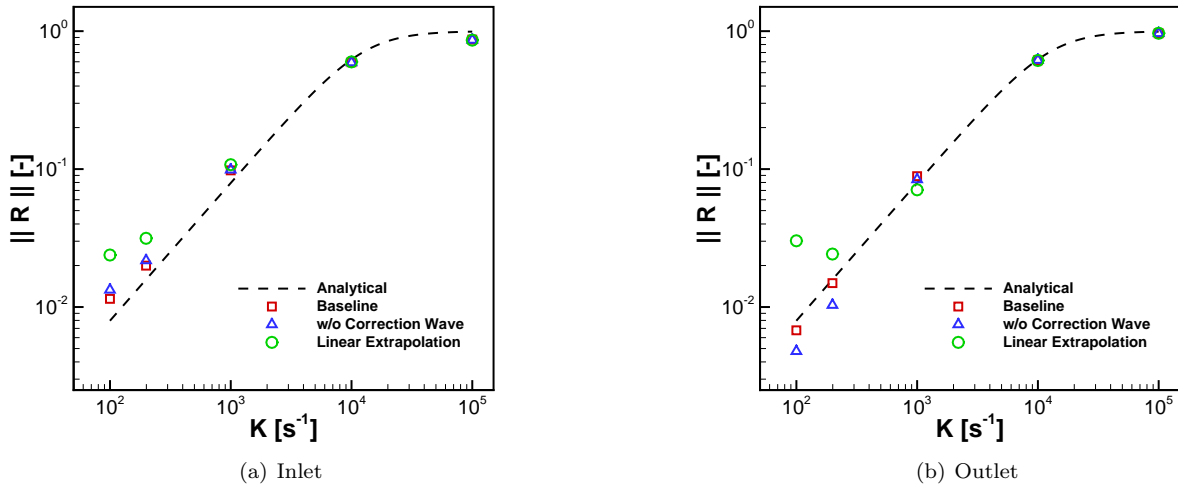


Figure 5. Reflection factor at inlet and outlet boundaries at $CFL=1$.

The reflection factor R depends on both the relaxation coefficient and the CFL number, as depicted by figure 6. Considering the baseline configuration (tab. 2), the reflection factor at an inlet boundary increases only slightly when the CFL number is increased from 1 to 5 (fig. 6(a)). Consequently, the predicted values still agree well with the analytical solution. However, at $CFL = 10$ (fig. 6(b)) the predicted reflection factor is at maximum one order of magnitude higher than the analytical value. Figure 6 shows also the impact of the correction wave discussed in section III.C. Turning off the correction wave leads to an additional overestimation of the reflection factor at $K = 10^2$ by a factor of around 2.

IV.D. Entropy Wave Generator (EWG) Test Case

Bake et al.¹⁰ analysed the generation of indirect combustion noise by means of the generic Entropy Wave Generator (EWG) test case. Figure 7 shows a sketch of the test rig which is basically a convergent-divergent nozzle flow. Entropy modes are generated by heating wires located upstream of the nozzle. These entropy

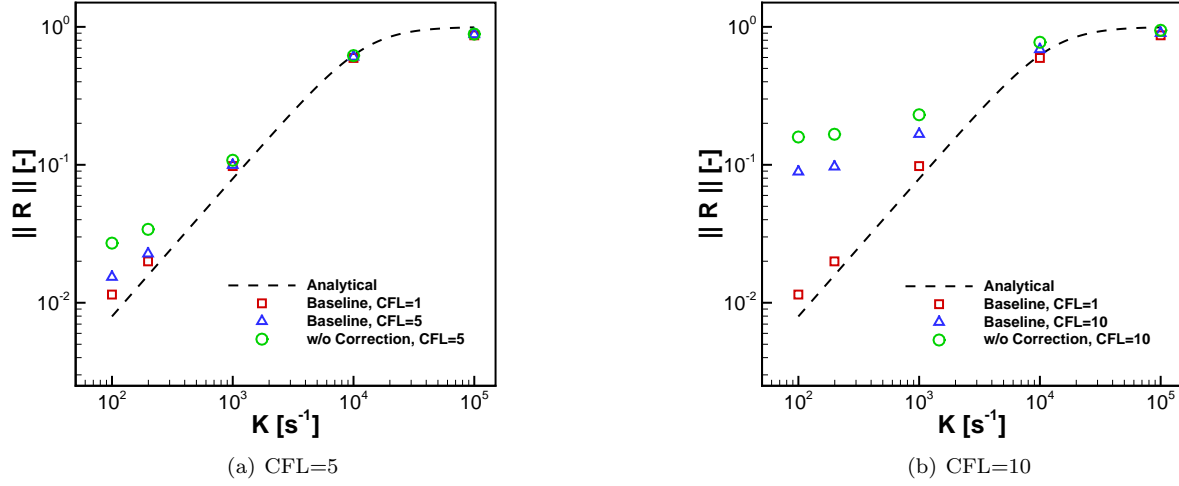


Figure 6. Reflection factor at the inlet boundary for different CFL numbers.

modes are convected and accelerated through the nozzle, which gives rise to pressure fluctuations downstream of the nozzle.

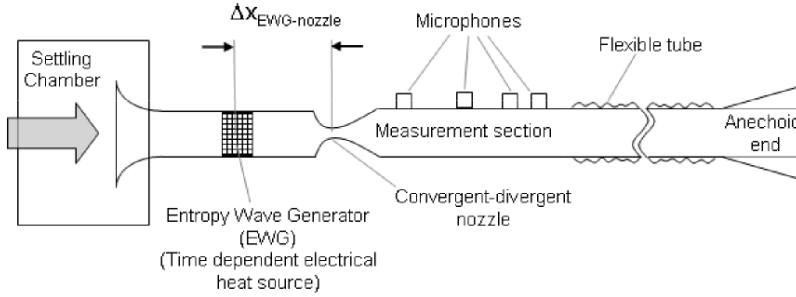


Figure 7. Sketch of the Entropy Wave Generator test rig.¹⁰

Table 3 summarises the geometrical dimensions of the analysed test case. All axial positions are measured from the most downstream heating wire. Further details are given by Bake et al.¹⁰ and Mühlbauer et al.²⁵ The heating power is adjusted to give a temperature increase of around $\Delta T \approx 9 \text{ K}$. Temperature fluctuations are measured by means of a bare wire thermocouple located between the heating module and the nozzle. Moreover, pressure fluctuations are gained at four positions downstream of the nozzle (tab. 3).

Table 3. Dimensions of EWG test case.¹⁰

Device	Axial Position [mm]	Diameter [mm]
Thermocouple	34	
Nozzle	105.5	7.5
Microphone 1	456	
Microphone 2	836	
Microphone 3	1081	
Microphone 4	1256	

For this discussion, numerical simulations with the DLR THETA code are carried out for different mass flow rates between 6 and 30 kg/h. Due to the rotational symmetry of the test rig, only a 10° slice of the flow is simulated. This slice is discretised by around 125 k grid points. The momentum and turbulence transport equations are spatially discretised by means of a second order quadratic upwind scheme (QUDS), whereas

all remaining equations are discretised centrally (CDS). Turbulent fluctuations are modeled by means of $k - \omega$ SST turbulence model.²⁶ Acoustic perturbations at frequencies lower than 3 kHz are resolved with at least 50 PPW, which gives very low dispersion and dissipation errors (sec. IV.B). As shown by Bake et al.,¹⁰ the acoustic impedance of the downstream termination of the flexible tube section of the test rig (fig. 7) can be modeled by means of characteristic boundary conditions. Applying a coupling parameter of $\sigma = 1.8$ at the downstream termination reproduces the experimentally measured pressure fluctuations accurately.^{10,25} Therefore, this value of the coupling parameter is also used for the computations presented in this discussion. Furthermore, data computed with ANSYS CFX 11.0 are used as validation of the THETA results. These data are provided by B. Mühlbauer and it was shown that they agree very well with the measurements of Bake et al.¹⁰ The corresponding numerical setup is described in detail by Mühlbauer et al.²⁵

Figure 8 shows the steady pressure and velocity distributions along the center line of the EWG nozzle for different nozzle Mach numbers. The plotted axial range corresponds roughly to the distance between the heating module ($x = 0$ mm) and the most upstream microphone ($x = 456$ mm). The pressure distributions predicted with THETA and CFX illustrated in figures 8(a) to 8(c) agree well. The maximum difference between both numerical solutions is visible for a nozzle Mach number of $Ma = 0.56$, where the predicted minimum pressures within the nozzle deviate by around 9 %. Moreover, THETA results show a slightly higher pressure of around 5 % upstream of the nozzle for all Mach numbers.

Besides the discussed pressure distributions, steady velocity distributions computed with THETA and CFX are illustrated in the lower row of figure 8. Both numerical solutions agree well for all plotted Mach number cases. The main differences between the velocity distributions are visible downstream of the nozzle, i.e. at $x > 0.1$. These deviations might result from different grid resolutions in the nozzle regime or from different discretisations of the transport equations used in THETA and CFX calculations. Both measures can lead to different boundary layer thicknesses downstream of the nozzle, and hence to different velocity distributions.

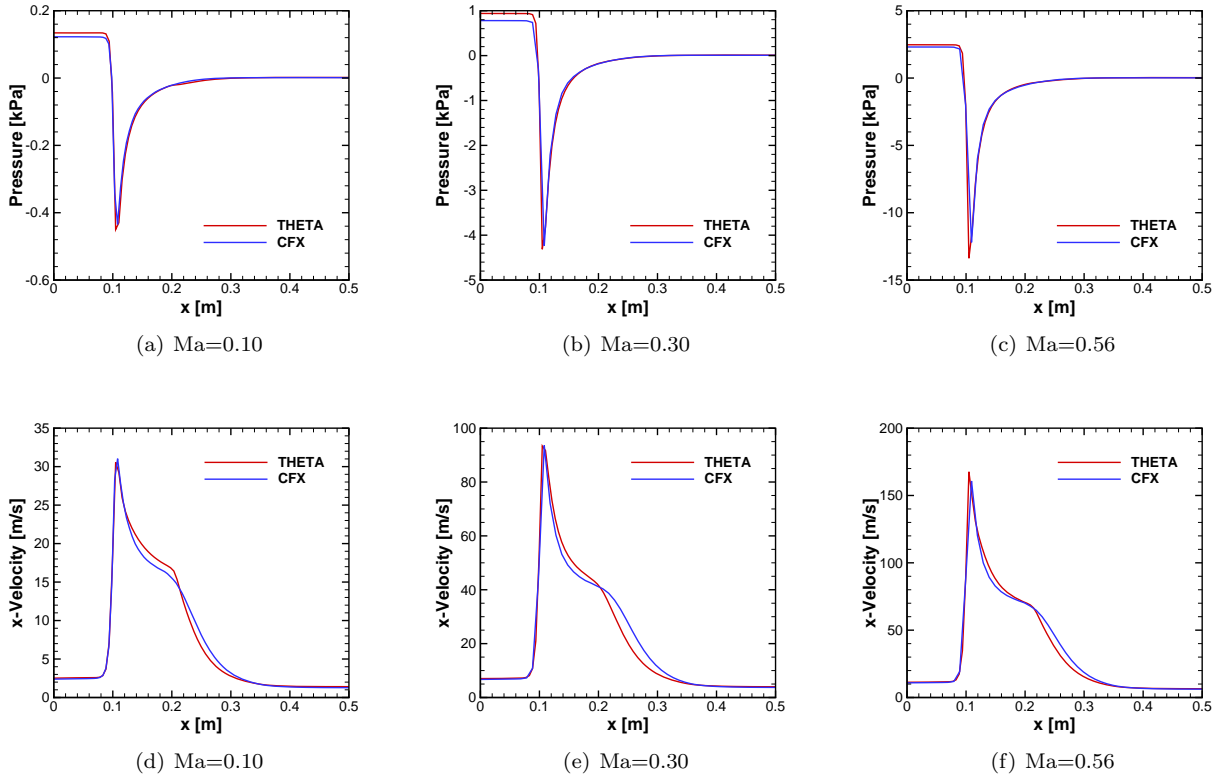


Figure 8. Steady results along EWG center line for different nozzle Mach numbers.

In case of the EWG, entropy waves are generated upstream of the nozzle by means of heating wires, which are turned on for $\Delta t = 0.1$ s.¹⁰ Convecting these modes through the nozzle results in pressure fluctuations downstream of the nozzle. Figure 9 shows the spectra of these fluctuations at the most downstream micro-

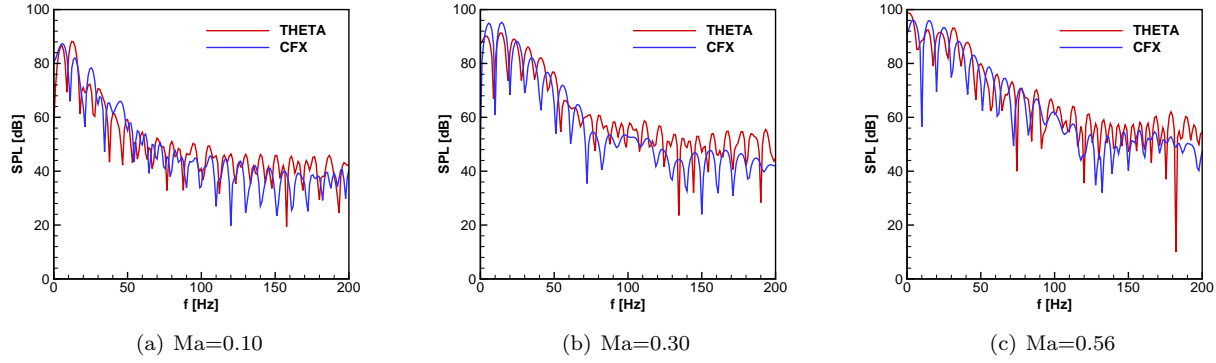


Figure 9. Spectra of the predicted pressure signals for different nozzle Mach numbers.

phone ($x = 1256$ mm) calculated with ANSYS CFX and DLR THETA. The spectra are obtained by discrete Fourier transform (DFT) from pressure signals with a sampling rate of 5 kHz. The numerical pressure signals are extended from a sampling time of 0.2 s to 0.9 s by zero padding to achieve a higher resolution in the low frequency range.²⁵ Furthermore, this leads to a better comparability with experimental results of Bäke et al.,¹⁰ which are also sampled over the extended time range. Figures 9(a) to 9(c) reveal that the most dominant pressure signals are in the lower frequency range of $f \leq 100$ Hz. Within this frequency regime both numerical solutions agree well for all nozzle Mach numbers. At higher frequencies, the pressure signals computed with THETA are slightly higher than the CFX results. Moreover, comparing the plotted pressure spectra shows that the sound pressure levels (SPL) increase with rising nozzle Mach numbers. Increasing the nozzle Mach number from 0.1 to 0.56 leads to an increase of the maximum SPL from around 88 dB to 94 dB (fig. 9(a) and 9(c)). Besides the increase in maximum SPL, the bandwidth of dominant pressure signals gets wider with increasing Mach number.

The growing SPL with rising nozzle Mach number is also visible in figure 10 which shows the maximum pressure fluctuation measured at the most downstream microphone ($x = 1256$ mm). Experimental and numerical data show that the maximum pressure fluctuation increases with the nozzle Mach number. Rising the nozzle Mach number from 0.1 to 0.56 leads to an increase of the maximum pressure fluctuation of around 16 Pa. Both numerical results, i.e. CFX and THETA data, are in good agreement with the experimental data. The pressure fluctuations computed with THETA agree slightly better with the experiments, especially in case of lower Mach number flows.

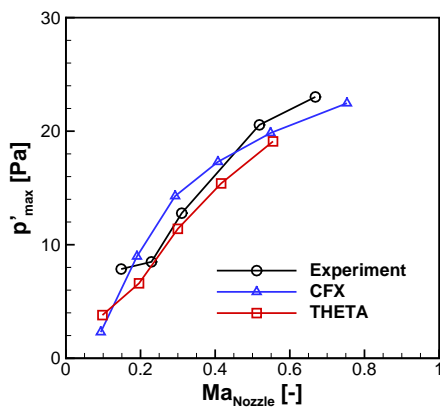


Figure 10. Maximum pressure fluctuation over the nozzle Mach number.^{10,25}

V. Conclusion

Computational fluid dynamics has become a promising tool to predict thermoacoustic instabilities in gas turbine combustion chambers. Within the scope of application, pressure based flow solvers are commonly used due to their high efficiency, i.e. low computational costs.⁴ In this work, the implementation of a pressure based fractional step method for compressible flows proposed by Moureau et al.³ in the DLR THETA code is discussed. Different implementation variants for the pressure correction equation and its boundary conditions are shown, and their impact on the convergence and accuracy of the algorithm is discussed.

The Laplacian of the pressure correction equation is discretised by a deferred approach in a partially or fully implicit way. As a result, a fully implicit discretisation leads to a better convergence, i.e. less iterations of the linear solver are required to meet a certain convergence criterion. Furthermore, the impact of the discretisation of convective terms on acoustic dispersion and dissipation is analysed. Two classical second order spatial discretisation schemes, namely quadratic upwind (QUDS) and central differencing (CDS) schemes, are compared to second order Lax-Wendroff, second order Total Variation Diminishing (TVD) and fifth order Weighted Essentially Non-Oscillatory (WENO) schemes.^{4,9} First of all, discretising with QUDS or CDS leads to almost equal acoustic errors. Furthermore, both schemes show comparable dissipation and dispersion errors to the Lax-Wendroff scheme in a resolution range of 10 to 40 points per wave length (PPW). In case of well resolved acoustic waves, i.e. with 40 PPW, the lowest dispersion and dissipation is visible in case of the fifth order WENO scheme. At this resolution, the dispersion is only around 2 times and the dissipation around 3.5 times higher with second order CDS and QUDS. This shows, that both schemes, i.e. QUDS and CDS, are appropriate discretisations to resolve acoustic perturbations in combustion chambers.

Besides the discretisation of the pressure correction equation, the implementation of characteristic boundary conditions is presented. In contrast to the standard approach, the characteristic equations are not solved explicitly at the boundaries. Hence, the algorithm does not suffer from acoustic CFL limitation at the boundaries. In this context, a new extrapolation approach based on the Green-Gauss method and a correction wave are presented. Using these additional measures leads to comparable accuracy to the standard approach of characteristic boundary conditions. Furthermore, the influence of the CFL number on the accuracy of the boundary conditions, i.e. on the reflection factor, is analysed. As a result, at a CFL number of two the accuracy is only reduced slightly, whereas at a $CFL = 10$ the reflection factor is overestimated at maximum by one order of magnitude.

As a validation, results of a generic test case for indirect combustion noise, the Entropy Wave Generator (EWG) test case by Bake et al.,¹⁰ are discussed. The test case consists basically of a convergent-divergent nozzle flow. Entropy modes, which are generated by heating wires upstream of the nozzle, lead to pressure perturbations measured downstream of the nozzle. Steady pressure and velocity distributions computed with DLR THETA and the commercial software ANSYS CFX are in good agreement. Furthermore, the impact of different nozzle Mach numbers on unsteady pressure fluctuations is analysed. A constant temperature increase of 9 K upstream of the nozzle leads to growing pressure fluctuations downstream of the nozzle with rising nozzle Mach number. Comparing the unsteady pressure spectra reveals that ascending the nozzle Mach number from 0.1 to 0.6 leads to an increase of the maximum SPL from around 88 dB to 94 dB. Moreover, the most dominant pressure signals are visible at frequencies below 100 Hz for all analysed cases with different nozzle Mach numbers. In this frequency regime, the pressure spectra computed with THETA and CFX agree well. Finally, the maximum pressure fluctuation is shown as a function of the nozzle Mach number. Data calculated with THETA show that the maximum pressure fluctuation increases by around 16 Pa when the nozzle Mach number is raised from 0.1 to 0.6. This result is confirmed by both CFX and experimental data.

VI. Acknowledgments

The authors would like to acknowledge B. Mühlbauer for providing the data computed with ANSYS CFX. The work presented was mainly performed in the frame of the DLR project IVTAS. Part of the financial support has also been provided by the Landesstiftung Baden-Württemberg within the scope of a research contract of the DLR for the State of Baden-Württemberg.

References

- ¹Moeck, J., Bothien, M., Schimek, S., Lacarelle, A., and Paschereit, C., "Subcritical thermoacoustic instabilities in a premixed combustor," *AIAA Paper 2008-2946*, 2008.
- ²Lieuwen, T. and Yang, V., *Combustion instabilities in gas turbine engines: operational experience, fundamental mechanisms and modeling*, AIAA Inc., 2005.
- ³Moureau, V., Bérat, C., and Pitsch, H., "An efficient semi-implicit compressible solver for large-eddy simulations," *J. Comput. Phys.*, Vol. 226, No. 2, 2007, pp. 1256–1270.
- ⁴Gunasekaran, B. and McGuirk, J. J., "Mildly-compressible pressure-based CFD methodology for acoustic propagation and absorption prediction," *Proceedings of ASME Turbo Expo 2011*, 2011.
- ⁵Chorin, A., "Numerical solution of the Navier-Stokes equations," *Mathematics of Computation*, Vol. 22, No. 104, 1968, pp. 745–762.
- ⁶Kim, J. and Moin, P., "Application of a fractional-step method to incompressible Navier-Stokes equations," *Journal of Computational Physics*, Vol. 59, No. 2, 1985, pp. 308–323.
- ⁷Pierce, C., *Progress-Variable Approach for Large-Eddy Simulation of Turbulent Combustion*, Ph.D. thesis, Stanford University, 2001.
- ⁸Di Domenico, M., *Numerical Simulation of Soot Formation in Turbulent Flows*, Ph.d. thesis, University of Stuttgart, 2008.
- ⁹Föller, S. and Polifke, W., "Determination of Acoustic Transfer Matrices via Large Eddy Simulation and System Identification," *16th AIAA/CEAS Aeroacoustics Conference*.⁴
- ¹⁰Bake, F., Richter, C., Mühlbauer, B., Kings, N., Röhle, I., Thiele, F., and Noll, B., "The Entropy Wave Generator (EWG): A reference case on entropy noise," *Journal of Sound and Vibration*, 2009.
- ¹¹Thompson, K., "Time Dependent Boundary Conditions for Hyperbolic Systems," *Journal of Computational Physics*, Vol. 68, 1986, pp. 1–24.
- ¹²Khosla, P. and Rubin, S., "A diagonally dominant second-order accurate implicit scheme," *Computers and Fluids*, Vol. 2, No. 2, 1974, pp. 207 – 209.
- ¹³Ferziger, J. and Peric, M., *Computational Methods for Fluid Dynamics*, 2002.
- ¹⁴Zwart, P., Raithby, G., and Raw, M., "An integrated space-time finite-volume method for moving-boundary problems," *Numerical Heat Transfer, Part B: Fundamentals*, Vol. 34, No. 3, 1998, pp. 257–270.
- ¹⁵Traore, P., Ahipo, Y. M., and Louste, C., "A robust and efficient finite volume scheme for the discretization of diffusive flux on extremely skewed meshes in complex geometries," *Journal of Computational Physics*,¹⁴ pp. 5148–5159, pp. 5148–5159.
- ¹⁶Blazek, J., *Computational fluid dynamics: principles and applications*, Vol. 1, Elsevier, 2005.
- ¹⁷Widenhorn, A., Noll, B., and Aigner, M., "Accurate Boundary Conditions for the Numerical Simulation of Thermoacoustic Phenomena in Gas-Turbine Combustion Chambers," *ASME Turbo Expo 2006*, 2006, pp. 1–10.
- ¹⁸Poinsot, T. and Veynante, D., *Theoretical and numerical combustion*, RT Edwards, Inc., 2005.
- ¹⁹Poinsot, T. and Lele, S., "Boundary Conditions for Direct Simulations of Compressible Viscous Flows," *Journal of Computational Physics*, Vol. 101, 1992, pp. 104–129.
- ²⁰Kreiss, H.-O., "Boundary conditions for hyperbolic differential equations," *Conference on the Numerical Solution of Differential Equations*, edited by G. Watson, Vol. 363 of *Lecture Notes in Mathematics*, Springer Berlin / Heidelberg, 1974, pp. 64–74.
- ²¹Selle, L., Nicoud, F., and Poinsot, T., "Actual impedance of nonreflecting boundary conditions: implications for computation of resonators," *AIAA journal*, Vol. 42, No. 5, 2004, pp. 958–964.
- ²²Meister, A., *Numerik linearer Gleichungssysteme*, Vieweg, Wiesbaden, 3rd ed., 2008.
- ²³Schoenfeld, T. and Rudgyardt, M., "Steady and unsteady flow simulations using the hybrid flow solver AVBP," *AIAA journal*, Vol. 37, No. 11, 1999, pp. 1378–1385.
- ²⁴Rudy, D. and Strikwerda, J., "A Nonreflecting Outflow Boundary Condition for Subsonic Navier-Stokes Calculations," *Journal of Computational Physics*, Vol. 36, 1980, pp. 55–70.
- ²⁵Mühlbauer, B., Noll, B., and Aigner, M., "Numerical investigation of the fundamental mechanism for entropy noise generation in aero-engines," *Acta Acustica united with Acustica*, Vol. 95, No. 3, 2009, pp. 470–478.
- ²⁶Menter, F., "Two-equation eddy-viscosity turbulence models for engineering applications," *AIAA Journal*, Vol. 32, No. 8, 1994, pp. 1598–1605.